Comparison of X-Ray and Neutron Thermal Parameters

The recent work of Coppens, *et al.*,[5,6] has shown that aspherical features in difference Fourier maps are obscured when only X-ray data are used, mainly because the atomic thermal parameters are increased in order to simulate bonding and lone-pair denisty which is not accounted for in the spherical atom scattering factor formalism normally used to refine a crystal structure. Similar conclusions can be drawn from our experiments by an examination of Table II, where we present the components of the anisotropic thermal tensors. It can be seen that in all cases the diagonal elements as derived from the neutron experiment are significantly smaller than the X-ray values by as much as nine combined standard deviations.

Table II. Some X-Ray and Neutron Thermal Parameters B_{ij} ($\times 10^4$)[a]

		X-Ray	Neutron	Δ	Δ/σ
O	11	110 (1)	94 (4)	16 (4)	4.0
	22	242 (3)	198 (12)	44 (12)	3.7
	33	75 (1)	66 (3)	9 (3)	3.0
	12	18 (1)	24 (6)	−8 (6)	
	13	10 (1)	0 (3)	10 (3)	
	23	24 (1)	26 (5)	−2 (5)	
C(1)	11	118 (2)	109 (4)	9 (4)	2.3
	22	196 (3)	168 (9)	28 (10)	2.8
	33	72 (1)	54 (2)	18 (2)	9.0
	12	9 (2)	2 (5)	7 (5)	
	13	42 (1)	31 (2)	11 (2)	
	23	4 (2)	−27 (4)	31 (4)	
N(3)	11	155 (2)	121 (3)	34 (4)	8.5
	22	354 (4)	294 (9)	60 (10)	6.0
	33	98 (1)	89 (2)	9 (2)	4.5
	12	−66 (3)	−75 (5)	11 (6)	
	13	50 (1)	38 (2)	12 (2)	
	23	−21 (2)	−24 (4)	3 (4)	
C(6)	11	100 (2)	88 (3)	12 (4)	3.0
	22	198 (3)	171 (8)	26 (9)	2.9
	33	55 (1)	40 (2)	15 (2)	7.5
	12	−9 (2)	−13 (5)	4 (4)	
	13	20 (1)	18 (2)	2 (2)	
	23	2 (1)	1 (4)	1 (4)	

[a] The atom numbering is that used in ref 3.

Conclusion

We have demonstrated the usefulness of combined X-ray and neutron scattering experiments for the experimental study of electron charge density distributions in molecular crystals and specifically in TCEO, where strong evidence has been obtained for the existence of a bent endocyclic C–C bond. Additional studies of these densities in both real and reciprocal space are currently in progress in order to compare independently measured functions of charge density distributions such as the dipole moment with those calculated from our experiments.

Electrogenerated Chemiluminescence. V. The Rotating-Ring–Disk Electrode. Digital Simulation and Experimental Evaluation

J. T. Maloy, Keith B. Prater, and Allen J. Bard*[1]

Contribution from the Department of Chemistry, The University of Texas at Austin, Austin Texas 78712.
Received January 13, 1971

Abstract: The rotating-ring–disk electrode (rrde) was used to generate the radical ion precursors of electrogenerated chemiluminescence (ecl). A cell assembly was designed to allow solutions to be degassed under vacuum and allowed the rrde to function in an inert atmosphere with the simultaneous performance of electrochemical and spectroscopic experiments. Digital simulation techniques have been employed to treat ecl at the rrde. The simulations predict the effect of rrde rotation rate and the kinetics of the radical ion annihilation reaction on the intensity of ecl light. When this annihilation reaction is very fast, *i.e.*, greater than $10^7\ M^{-1}\ \text{sec}^{-1}$ for the rrde used here, the ecl is seen as a sharp ring of light at the inner edge of the ring electrode, and its intensity, like the disk current, is proportional to the square root of rotation rate. The simultaneous measurement of steady-state disk current and ecl intensity as functions of the disk potential gives direct information about the role of any disk-generated species in the light-producing process. An evaluation of the technique using the ecl of 9,10-diphenylanthracene in *N*,*N*-dimethylformamide solution is described.

Electrogenerated chemiluminescence (ecl) studies are usually carried out at a single working electrode whose potential is varied to generate the reduced and oxidized species which react in the diffusion layer near the electrode to produce light.[2] While this method is simple experimentally and has been very useful in the elucidation of reaction mechanisms in ecl, it suffers from several disadvantages. Because of the repetitive switching at a single electrode, a fraction of the species produced during one half-cycle is consumed electrochemically during the next half-cycle. This makes it

(1) To whom correspondence and requests for reprints should be directed.

(2) This work has been reviewed in (a) A. J. Bard, K. S. V. Santhanam, S. A. Cruser, and L. R. Faulkner, "Fluorescence," G. G. Guilbault, Ed., Marcel Dekker, New York, N. Y., 1967, Chapter 4; (b) D. M. Hercules, *Accounts Chem. Res.*, 2, 301 (1969).

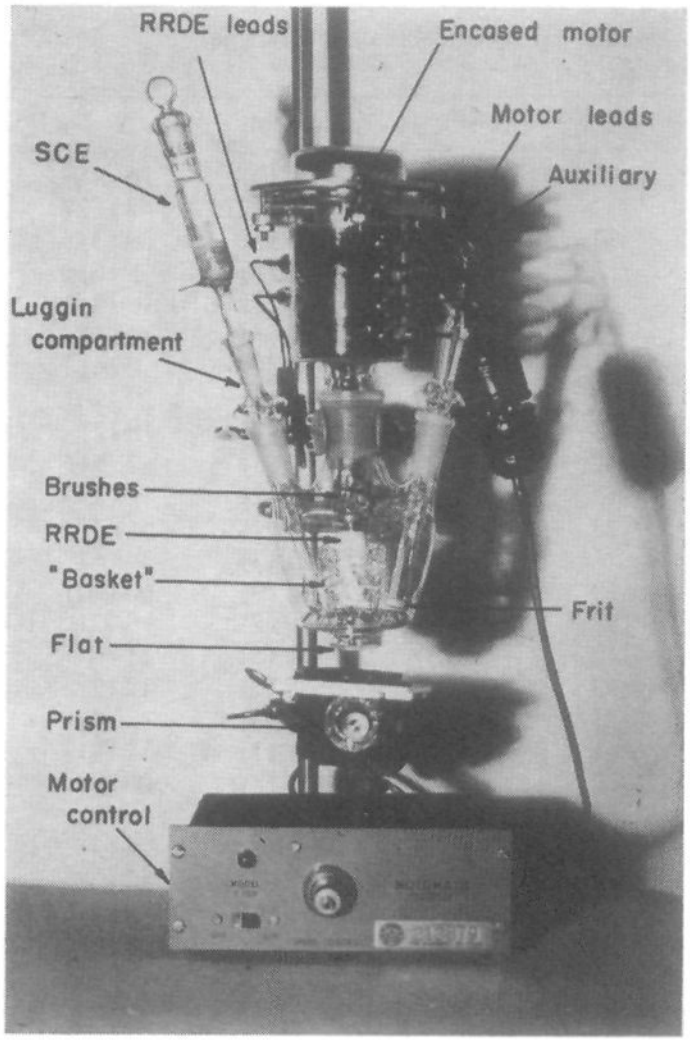

Figure 1. The rotating-ring–disk electrode and cell assembly.

difficult to estimate the overall efficiency (photons emitted per annihilation reaction) of the process. Moreover, small amounts of reaction side products tend to accumulate in the vicinity of the electrode. Finally, no steady-state light levels can be obtained at a single electrode. These difficulties can be surmounted by producing the oxidized and reduced species at separate electrodes and rapidly flowing these together. This is most conveniently carried out, considering that deoxygenated and highly purified solutions must be employed, by the use of the rotating-ring–disk electrode (rrde),[3] employing the disk electrode to generate one species and the ring electrode to generate the other. A preliminary account of ecl studies at the rrde has been described.[4] This paper deals with a detailed description of the theoretical treatment of the process and a description of the experimental methods employed. A second paper in this series[5] describes the results of ecl studies on several different systems.

Experimental Section

The chemicals used and purification procedures employed have been described previously.[6] Great care was taken to ensure the purity of solvent and solution components; at no time was inexplicable (*i.e.*, unaccompanied by two measurable electrode processes) or "preannihilation" ecl emission observed from fresh solutions.

The rrde used was manufactured by the Pine Instrument Co. (Grove City, Pa.). The dimensions of the platinum ring and disk were: $r_1 = 0.145$ cm = radius of the disk, $r_2 = 0.163$ cm = inner radius of the ring, $r_3 = 0.275$ cm = outer radius of the ring. The platinum ring and disk were embedded into the Teflon to a depth of 0.3 cm; this is approximately twice the normal thickness of platinum used in the manufacture of the rrde, and it was found to be necessary to ensure against solution leakage between the platinum and the insulator.

The rrde was driven with a Motomatic Model E150 tachometer-generator motor (Electrocraft Corp., Hopkins, Minn.) using feedback control. This motor was capable of being rotated at any preset rate up to 1000 radians/sec by means of a precalibrated speed control fitted with a ten-turn potentiometer. The added torque of the electrode and its brushes lowered the upper limit of the rotation rate to about 700 radians/sec in actual operation, but because feedback control was used, the linearity of response was unaffected up to that point. The electrode was attached to the motor shaft with a collet which was custom machined for this purpose.

The entire motor–electrode assembly was encased in a Pyrex motor mount. The motor mount consisted of a Pyrex cylinder having inside dimensions large enough to contain the motor. The top of the cylinder was flanged outward (desiccator fashion) to accommodate a similarly flanged lid; the bottom of the cylinder was closed except for a central standard-taper joint through which the electrode could pass freely. A Pyrex extension cylinder was attached to the lower end of this joint; small holes were drilled in this extension so that brushes could be anchored there with wires to make stationary contact with the rotating electrode.

The cylinder was also fitted with a simple disk clamp to hold the motor in position. Three coplanar protuberances were blown equidistant from each other in the upper interior wall of the cylinder. Three semicircular cuts were made in an aluminum disk of the same diameter as the interior wall of the cylinder so that it could just pass over these protuberances. This disk was drilled, tapped, and fitted with four machine screws. When the motor was in place, the disk could be slipped over the protuberances and rotated 60° so that it could not be removed; the four machine screws could then be tightened against the motor, thereby pressing it against the base of the cylinder and securing it firmly in place.

The motor–electrode assembly was encased in the motor mount by first fitting each brass electrode contact with a spiral brush hand wound from soft copper wire. Care was taken so that these were wound tight enough to provide continuous electrical contact as the electrode was rotated, yet loose enough not to hinder rotation seriously. Short leads were soldered to these brushes and these were temporarily wrapped around the shaft of the electrode. Then Teflon-insulated leads were soldered to the six contacts inside the cylinder. Four of these were soldered to the motor immediately; the remaining two were passed down through the joint where they were to be connected to the brush contacts for the ring and disk. A rubber O ring was placed on the bottom of the glass cylinder concentric with the hole made by the joint. This served as a shock-absorbing seat for the motor. The electrode, with the brushes attached, was passed down through the O ring and the joint until the motor rested on the O ring. The motor was then clamped in place with the disk clamp described previously. Only after the motor had been secured were the brush leads unwound from the electrode shaft which, with the motor in place, passed through the Pyrex extension at the lower end of the joint. These leads were then drawn through the small holes in the extension and held in place with beads of solder too large to permit the leads to go back through the holes. Thus, the brushes were held stationary in the proper position so that it was now possible to connect the two electrode leads which had been passed through the joint at the start of the assembly process.

Double O rings were placed around the flange at the top of the cylinder and the lid was clamped in place with a three-bolt circular clamp which pressed against both flanges. Prepared in this way, the motor–electrode assembly was completely encased in glass with the brushes held permanently in place. More importantly, the electrode was in a fixed position with respect to a standard joint, so that it was quite easy to place the electrode reproducibly. This motor mount proved to be quite air tight; given sufficient time to outgas the motor and its windings, one could achieve pressures of 10^{-4} Torr within it.

The assembled motor mount is shown in position in Figure 1, together with the entire cell assembly used for most of the rrde-ecl experiments. The male standard-taper joint of the motor mount fitted into the central joint of the cell so that the end of the electrode was less than 1 cm from the bottom of the cell. Because of space requirements, the cell itself had tapered sides so that it resembled a truncated cone; the two additional joints which were located at

(3) A. N. Frumkin, L. Nekrasov, V. G. Levich, and Y. B. Ivanov, *J. Electroanal. Chem.*, **1**, 84 (1959).
(4) J. T. Maloy, K. B. Prater, and A. J. Bard, *J. Phys. Chem.*, **72**, 4348 (1968).
(5) J. T. Maloy and A. J. Bard, *J. Amer. Chem. Soc.*, **93**, 5968 (1971).
(6) L. R. Faulkner and A. J. Bard, *ibid.*, **90**, 6284 (1968).

the top of the cell were inclined at this angle. One of these joints held a Luggin compartment which, in turn, held the saturated calomel electrode (sce) used as a reference; the tip of the Luggin compartment was placed as close as practically possible to the rrde and coplanar with it. The other joint held the auxiliary electrode compartment which, in turn, held the coiled platinum counter electrode; this compartment was fitted with a sintered glass frit at its base so that products made at the auxiliary electrode during electrolysis would be inhibited from entering the bulk solution. The rrde passed through a cylindrical "basket" made of crocheted glass. This "basket" was found to be effective in the supression of vortex formation as the electrode was rotated; its presence extended the useful range of rotation rates to the full capabilities of the motor. Finally, the cell was equipped with a vacuum-stopcocked standard ball joint so that it could be attached to the vacuum line; this stopcock cannot be seen in Figure 1.

Chemiluminescent emission generated at the rrde passed through a Pyrex flat mounted beneath the electrode. This flat was attached to a short cylinder of Pyrex which extended from the base of the cell to fit into a circular cavity at the top of a turret-mounted reflecting prism; this greatly facilitated reproducible cell placement. The prism was turret mounted in a platform which was designed to be placed in the cell cavity of an Aminco-Bowman spectrophotofluorometer where it could be raised or lowered and the turret could be rotated to obtain optimum reflection of emission. After this optimum set of reflecting conditions had been found, the elevation of the platform and the turret angle were fixed so that these positions were always the same. The insertion of the turret-mounted prism into the spectrophotofluorometer cavity necessitated the removal of the cell holder supplied by the manufacturer; hence, two of the four emission slits normally present in fluorescence spectroscopy were absent in these ecl experiments. One-millimeter slits were used exclusively in the remaining two slit positions, and these were sufficient to produce spectra which were fairly well defined.

Because of the intricate nature of this cell design, it was thought unwise to subject it to the thermal stresses of the freeze–pump–thaw technique. Therefore, a device (Figure 2) was designed which permitted the solution to be degassed separately and then transferred into the cell under an inert helium atmosphere. This device is nothing more than a cold trap which has been rendered rotatable with judiciously placed ball and socket joints. When placed in an intermediate position between the vacuum line and the cell, it was used either to hold a solution for degassing in the position illustrated or to deliver the solution to the cell after a rotation through an angle of 180°. With no solution in it, it could be rotated freely under vacuum with no detectable change in gauge pressure (10^{-4} Torr); hence, there was no reason to suspect leakage at the joints during rotation.

In a typical experiment, the empty device was mounted between the cell assembly and the vacuum line; the cell assembly was that shown in Figure 1, except that the Luggin compartment was sealed with a glass stopper. The cell was pumped out through the device, and after sufficient evacuation (10^{-3} Torr) it was filled with 1 atm of helium and sealed. A solution was then introduced into it where it was degassed under vacuum by repeatedly freezing it with liquid nitrogen and allowing it to thaw after the pressure reached 10^{-4} Torr. Each solution was subjected to a minimum of three such freeze–pump–thaw cycles. After the solution had been degassed, the stopcock leading to the cell assembly was opened and the entire line was evacuated to the vapor pressure of the solution. Helium was reintroduced, but this time the cell stopcock was closed when the helium pressure was slightly less than 1 atm within the cell assembly; the helium pressure within the device was allowed to reach 1 atm, however, so that it was at a pressure slightly positive to that of the cell. Then the device was inverted and the cell stopcock was opened so that the solution was delivered under pressure to the cell. When the helium pressure in the cell had been brought up to 1 atm, the cell stopcock was closed and the cell assembly was removed from the line so that it could be manually rotated to fill the Luggin compartment and the auxiliary compartment through small interior holes provided for this purpose near the top of each compartment. The assembly was then returned to the line so that helium could be passed over the solution as the Luggin compartment was opened and the cell was fitted with the sce. When this had been accomplished, the stopcock was closed again and the cell was ready for use.

Electrochemical experiments at an rrde are usually performed with a dual-channel potentiostat.[7] However, the high internal

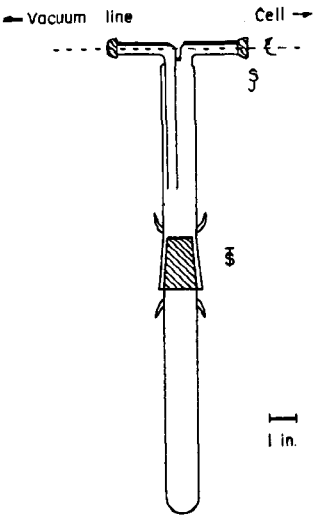

Figure 2. Device for preparation and degassing of solutions on vacuum line prior to introduction into ecl cell.

resistances of the solutions used in these experiments were such that a potentiostat built according to this description would not independently potentiostat both ring and disk (although it worked satisfactorily in aqueous solutions). This problem was resolved by potentiostating one electrode and controlling the potential or current at the other electrode manually with a battery and a variable resistor connected in series with it and the auxiliary electrode. In this configuration the potential of the battery-controlled electrode could be determined with a high-impedance digital voltmeter (Fairchild Model 7050) connected directly between the electrode and the reference electrode; the current at that electrode could be determined from the voltage drop across a measuring resistor in series with it. The type of experiment to be performed determined whether the ring or the disk was to be battery operated.

Digital Simulations

Methods. Digital simulation techniques have been used to treat a variety of electrochemical,[8] ecl,[9] and rrde[10] problems. The extension of the digital simulation method to the problem of rrde ecl is fairly straightforward. In fact, the computer programs written by Prater[11] to treat rrde problems need only slight modification to treat rrde ecl. Hence, only their modifications will be discussed in detail.

In treating rrde ecl with digital simulation, one models the hydrodynamic layer of the solution by dividing it into a specified number of volume elements; the concentration of any species in solution is considered to be uniform within a given element. Owing to the cylindrical symmetry of the rrde, the solution is divided into several layers of thickness Δx with each layer containing a cylindrical element of diameter Δr which is centered on the axis of rotation; a series of concentric annular elements each of thickness Δr make up the remainder of each layer. Each element is numbered with its layer number, J, and its radial number, K; hence, the fractional concentration of any species (its real concentration divided by the bulk concentration of a species

(7) D. T. Napp, D. C. Johnson, and S. Bruckenstein, *Anal. Chem.*, 39, 481 (1967).

(8) S. W. Feldberg in "Electroanalytical Chemistry," Vol. 3, A. J. Bard, Ed., Marcel Dekker, New York, N. Y., 1969, Chapter 4, and references contained therein.

(9) (a) S. W. Feldberg, *J. Amer. Chem. Soc.*, 88, 390 (1966); (b) S. A. Cruser and A. J. Bard, *ibid.*, 91, 267 (1969).

(10) K. B. Prater and A. J. Bard, *J. Electrochem. Soc.*, 117, 207, 335, 1517 (1970).

(11) K. B. Prater, Ph.D. Dissertation, The University of Texas at Austin, 1969.

present initially) is specified as a function of two integers. Thus, in the nomenclature used by Prater, $F_B(J, K)$ is "the fractional concentration of the Bth species in the Jth layer and the Kth ring."

The diffusion, convection, and the chemical reactions (kinetics) of the species which occupy these elements are also functions of time. These temporal changes are modeled iteratively, each interaction of duration Δt generating a new two-dimensional concentration array for each species present. The algorithms used to handle each of these changes are given by Prater. Normal diffusion is treated by a difference method; radial diffusion is neglected. Both normal and radial convection are simulated by using the laws of hydrodynamics to calculate the distance the solution in a given volume element travels during the interval Δt; a new array is generated by effecting these translations for each element. Chemical reactions occurring during Δt are treated by using the difference equation form of the differential rate law to calculate new concentrations within each element following each iteration.

Variables of electrochemical interest are specified by the electrode boundary conditions that give rise to the concentration gradients in solution. Current is measured as the flux of electroactive material into the electrode under a given set of potential-dependent electrode conditions. While it is easy to simulate any reversible-electrode potential or any magnitude of constant current, the simulations reported herein all assume a potential such that the concentration of the electroactive species goes to zero at the electrode and the limiting current is achieved.

Obviously, the validity of any such simulation will depend upon the dimensions of Δx, Δr, and Δt; as these approach zero, the problem approaches differential form. Making these smaller, however, increases the computational time required to achieve a steady state solution; therefore, some optimization is required. In practice, these incremental quantities are defined at the outset of the simulation in terms of real time–distance parameters and dimensionless quantities which are specified within the program. For example, Δx is defined in terms of Δt and D_A, the diffusion coefficient of the species originally present in solution

$$\Delta x \equiv (D_A \Delta t / DM_A)^{1/2} \tag{1}$$

Here DM_A is the model diffusion coefficient of species A, and it is assigned a value less than 0.5. Similarly, Δt is defined in terms of ω, the angular velocity, D_A, and ν, the kinematic viscosity of the solvent

$$\Delta t \equiv (D_A/\nu)^{1/3} \omega^{-1} / L \tag{2}$$

where L is an assigned number of time iterations; it is found that after $3L$ iterations, steady-state conditions are achieved. Finally, Δr is defined by $IR1$, the number of elements which make up the disk electrode

$$\Delta r \equiv r_1/(IR1 - 0.5) \tag{3}$$

Thus, it may be seen that the specification of the variables DM_A, L, and $IR1$ simultaneously specifies Δx, Δt, and Δr. In the simulation reported below, the following values were used for each of these quantities: $DM_A = DM_B = DM_C = 0.45$, $L = 50$, and $IR1 = 81$. This set of input parameters is such that one steady-state simulation is obtained after 60 sec of computation with the Control Data Corp. Model 6600 computer; in cases where comparisons with "exact" solutions are possible (*e.g.*, disk current in the absence of kinetic complications), the simulated results obtained in this computation time are found to agree within the error of electrochemical measurement (*ca.* 1%).

Since the basic rrde program[10,11] calculates collection efficiencies, some modification of boundary conditions is required to treat rrde ecl according to the sequence of reactions

$$\mathrm{A} \longrightarrow \mathrm{B} \text{ (disk reaction)} \tag{4}$$

$$\mathrm{A} \longrightarrow \mathrm{C} \quad \mathrm{B} \longrightarrow \mathrm{C} \text{ (ring reactions)} \tag{5}$$

$$\mathrm{B} + \mathrm{C} \xrightarrow{k_2} \text{chemiluminescent products} \tag{6}$$

where A represents the parent species and B and C represent the electrogenerated radical ions. For the disk, these boundary conditions are unchanged by the introduction of C, the ring-generated species. They are

$$\begin{aligned} F_A'(1, 1) &= F_A(1, 1) = 0 \\ F_B'(1, 1) &= F_B(1, 1) + DM_A[F_A(2, 1)] - \\ &\qquad DM_B[F_B(1, 1) - F_B(2, 1)] \\ F_C'(1, 1) &= F_C(1, 1) = 0 \end{aligned} \tag{7}$$

where the primes refer to conditions that will exist at the start of the next iteration. Note that only one element is required to simulate the $IR1$ elements making up the disk electrode, and $K = 1$ in these equations; this is possible because the disk is a uniformly accessible surface in these experiments so that the same conditions would appear for each element. The quantity DM_A $[F_A(2, 1)]$ represents the amount of species A which is converted to B at the disk; this is proportional to the disk current.

Since the ring is not uniformly accessible, each ring element must be treated separately. The boundary conditions for each ring element become

$$\begin{aligned} F_A'(1, K_R) &= F_A(1, K_R) = 0 \\ F_B'(1, K_R) &= F_B(1, K_R) = 0 \\ F_C'(1, K_R) &= F_C(1, K_R) + DM_A[F_A(2, K_R)] + \\ &\quad DM_B[F_B(2, K_R)] - DM_C[F_C(1, K_R) - F_C(2, K_R)] \end{aligned} \tag{8}$$

where K_R is a radial element number of an element representing the ring. The current at the ring is proportional to the area-weighted sum of the currents of each ring element: $\Sigma(DM_A[F_A(2, K)] + 2DM_B[F_B(2, K)]) \cdot [A(K)/A_D]$, where $A(K)$ is the area of the Kth ring and A_D is the area of the disk. Note that the total current is the sum of current contributions from both species A and species B.

Diffusion and convection are treated just as in previous rrde simulations; therefore, the only remaining additional complication of the rrde-ecl simulation is the treatment of (6), the reaction of B and C to produce light. Species B and C, of course, are the radical ions of A, the hydrocarbon present initially; the reaction in question is an electron-transfer reaction which may or may not produce light.

$$\begin{aligned} \mathrm{B} + \mathrm{C} &\xrightarrow{k_2} {}^1\mathrm{A} + {}^1\mathrm{A}^* \\ {}^1\mathrm{A}^* &\longrightarrow {}^1\mathrm{A} + h\nu \end{aligned} \tag{9a}$$

or

$$\mathrm{B} + \mathrm{C} \xrightarrow{k_2} 2\,{}^1\mathrm{A} \tag{9b}$$

In any event, since the radiative conversion of the excited singlet to ground-state singlet is quite rapid, the net material effect of each fruitful encounter of B and C is the production of 2A, and the number of quanta produced depends upon the fraction of fruitful encounters of B and C which proceed by (9a). Therefore, it is convenient to define Φ_{ecl}, the efficiency of the ecl process, as the fraction of fruitful radial ion encounters which result in the emission of a photon.

With this background, one may rewrite the differential rate law

$$-\mathrm{d[B]}/\mathrm{d}t = k_2[\mathrm{B}][\mathrm{C}] \quad (10)$$

in difference form using fractional concentrations

$$-\Delta F_B(J, K) = (k_2 C_A^0 \Delta t) F_B(J, K) F_C(J, K) \quad (11)$$

where C_A^0 is the bulk concentration of A. Combination of (2) with (11) yields the form actually used in the simulation

$$-\Delta F_B(J, K) = [(D_A/\nu)^{1/3}(k_2 C_A^0/\omega)] F_B(J, K) F_C(J, K)/L \quad (12)$$

where the bracketed dimensionless coefficient is assigned the variable name *XKTC* in the simulation

$$XKTC = (D_A/\nu)^{1/3}(k_2 C_A^0/\omega) \quad (13)$$

This is the final variable input parameter used in the simulation of rrde ecl; variations in *XKTC* determine the extent to which rotation competes with kinetics.

Equation 12 is used to determine the chemical changes due to radical-ion reactions within each element and to quantify the chemiluminescence occurring as a result of these changes. The fractional concentrations in each element are adjusted accordingly during each iteration

$$\begin{aligned} F_A'(J, K) &= F_A(J, K) - 2\Delta F_B(J, K) \\ F_B'(J, K) &= F_B(J, K) + \Delta F_B(J, K) \\ F_C'(J, K) &= F_C(J, K) + \Delta F_B(J, K) \end{aligned} \quad (14)$$

The number of photons emitted from any element during Δt is given by $-\Delta F_B(J, K)\Phi_{ecl} C_A^0(\Delta x A(K))$ so that I, the total ecl intensity (in quanta per second), is the sum of the emission from all the elements divided by Δt

$$I = -\sum_{J,K}[\Delta F_B(J, K)\Phi_{ecl} C_A^0(\Delta x A(K))]/\Delta t \quad (15)$$

Substitution of (1), (2), and (13) into (15) and division of both members by A_D yields, after rearrangement

$$\frac{I}{\Phi_{ecl} A_D (D_A (C_A^0)^3 k_2)^{1/2}} = -\left(\frac{L}{XKTCDM_A}\right)^{1/2} \sum_{J,K} \Delta F_B(J, K) \frac{A(K)}{A_D} \quad (16)$$

where the right member contains only simulation variables and the left member is a dimensionless ecl parameter. Note that I is rendered dimensionless by k_2 rather than ω. To use digital simulation, then, to model the steady-state intensity–rotation rate dependence, one varies *XKTC*, the dimensionless representation of ω in the program described above, and obtains the steady-state parameter in (16) as a function of *XKTC*. A copy of the program used in these simulations is available.[12]

(12) J. T. Maloy, Ph.D. Dissertation, The University of Texas at Austin, 1970.

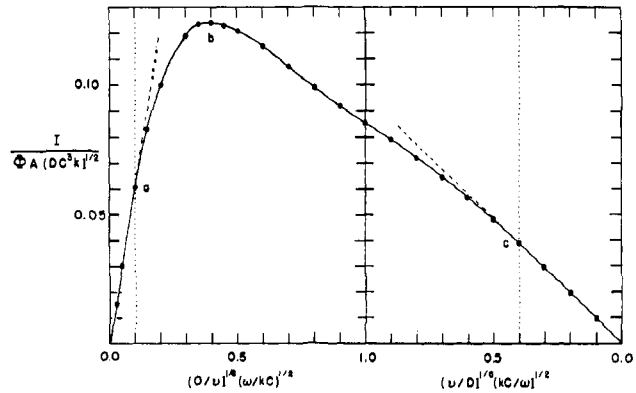

Figure 3. The simulated steady-state ecl intensity (normalized) at the rrde. Each point shown represents a separate digital simulation.

Results

The results of this simulation are displayed in Figure 3, which shows the variation of the dimensionless ecl parameter of (16) with the square root of the dimensionless ω parameter *XKTC*. Actually, Figure 3 consists of two graphs having the same ordinate and lying adjacent at a common point; the abscissa of the graph on the right, however, is the reciprocal of that on the left plotted in reverse. Hence, the total abscissa is drawn with ω increasing in a nonlinear fashion from left to right, and all possible values of ω are shown. The denominator of the ordinate variable contains only factors which are constants, given a set of experimental conditions; similarly, the abscissa variables can change only when ω changes in a real experiment, so that Figure 3 is the dimensionless representation of the I *vs.* ω behavior in rrde ecl. The simulation predicts that rrde ecl will increase with increasing rotation rate, go through a maximum, and decrease to zero thereafter. In fact, the maximum (point b on the graph) is predicted when

$$(D_A/\nu)^{1/6}(\omega/k_2 C_A^0)^{1/2} = 0.4 \quad (17)$$

or, since $(\nu/D_A) \approx 10^3$ for systems of electrochemical interest, when $\omega \approx 1.6 k_2 C_A^0$. Since the maximum rotation rate possible with the rrde system described here is about 10^3 sec^{-1} and the minimum practical concentration of species is about 1 mM, the ecl maximum will be reached only if k_2 is less than 10^6 M^{-1} sec^{-1}. In addition to point b, two additional points have been marked on Figure 3 and vertical lines passing through these points divide the graph into three regions. Interior to point a, the simulation predicts linear behavior with the straight line passing through the left origin; exterior to point c, a straight line passing through the right origin is predicted. This indicates that as I is increasing, it increases with $\omega^{1/2}$, but as it decreases, it decreases with $\omega^{-1/2}$. More importantly, it may be observed that, in theory, three distinctly different types of ecl behavior may be observed, depending upon whether the reaction kinetics are fast, slow, or intermediate with respect to the rotation rate.

Concentration contours at these three rotation rates (a, b, and c) are shown for species A and species C in Figure 4. These graphs depict lines of equal concentration within the region bounded by a radius of the electrode and the hydrodynamic layer to a thickness of 2δ where

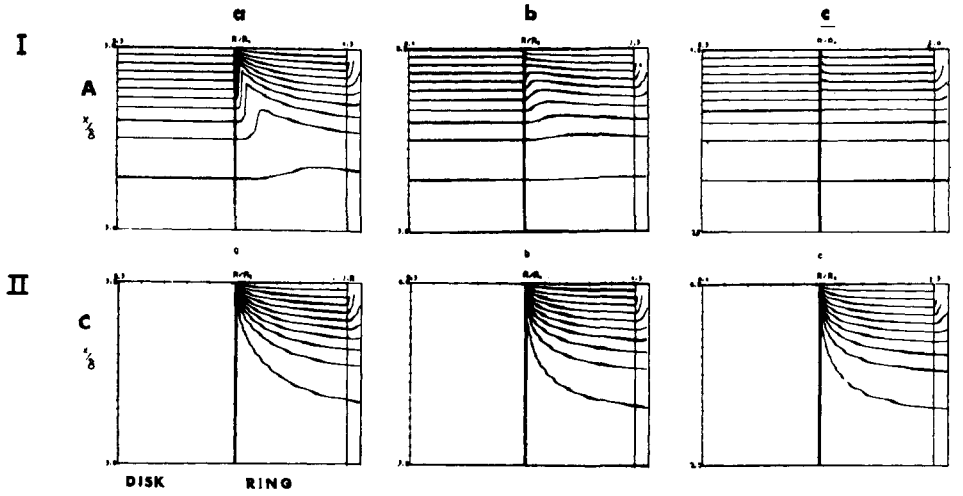

Figure 4. Concentration profiles at the rrde. Horizontal axis is r, the distance across rrde, representing (from left to right) disk region, very narrow gap region, ring region, and outside insulator region. Vertical axis is x, the distance perpendicular to rrde. Lines of equal fractional concentration are separated by 0.1 unit: I shows species A (parent) with 0.99 the outermost line; II shows species C (ring-generated species) with 0.01 the outermost line. a, b, and c refer to the points in Figure 3. For $(D/\nu) \sim 10^{-3}$, these correspond to the following values of (ω/kC): (a) 0.1, (b) 1.6, (c) 62.5.

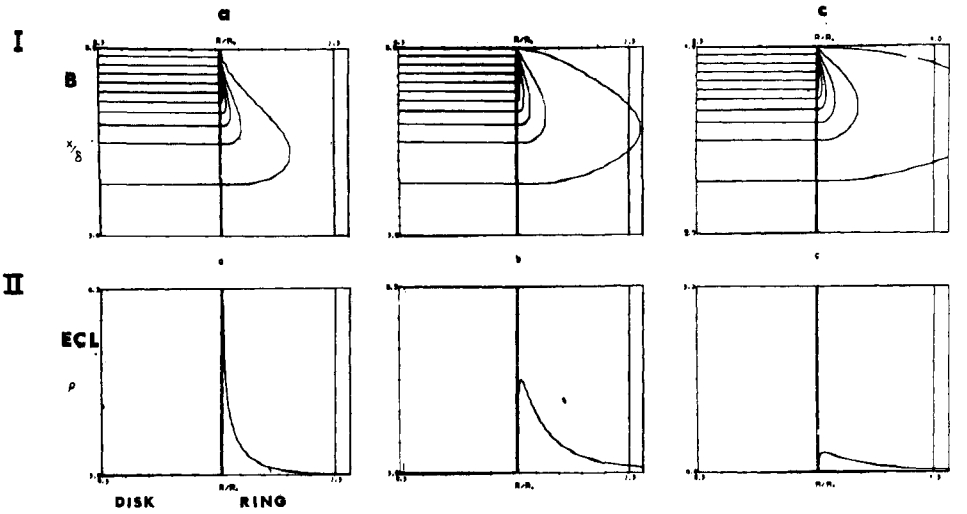

Figure 5. Concentration profiles and ecl density at the rrde. I shows species B (disk-generated species) with 0.01 the outermost line. II shows the light density across the electrode. Other information is given in the caption to Figure 4.

$$\delta = 1.8 D_A^{1/3} \nu^{1/6} \omega^{-1/2} \quad (18)$$

Three vertical lines partition the hydrodynamic layer (which is drawn here increasing in a negative direction) into areas below the disk, gap, ring, and shield of the electrode. The lines of equal concentration are drawn every 0.10 unit of fractional concentration. Part I of Figure 4 depicts species A so that the outermost (lowest) line is the line of 0.99 fractional concentration. In part II of Figure 4, species C is depicted with the outermost line of fractional concentration 0.01. These differences result, of course, because A is moving toward the electrode, whereas C is moving away from it. The simulation shows that the species generated at the ring (species C) surrounds the disk in a torus-like form. In part I of Figure 5, the concentration contours of species B are shown with the outermost line at a fractional concentration of 0.01. These contours really illustrate the effectiveness of the torus of C in blocking the penetration of B into the ring area. In part Ia of Figure 5 (fast kinetics), it is quite effective; in part Ic of Figure 5, much of the disk-generated species escapes into the bulk of the solution.

The effect of this on the ecl produced by the reaction of B and C is shown in Figure 5, part II, where ρ, the density of ecl emission (normal to the electrode), is shown as a function of electrode radius. At a, ecl would be seen as a sharp ring of light close to the inner edge of the ring. At b, the emission maximum would be displaced from the inner edge of the ring and the emission would be spread out, falling to about one-third of the maximum at mid-ring. Finally, at c, the chemiluminescence would almost appear to cover the ring uniformly. Therefore, the appearance of the ecl emission is indicative of the rate of the process relative to the rotation rate.

If the process is rapid, ecl will be observed as a bright ring at the innermost edge of the ring. This region of fast kinetics, as noted above, is a region where I increases with $\omega^{1/2}$ and obeys the equation

$$\frac{I}{\Phi_{ecl} A_D (D_A (C_A^0)^3 k_2)^{1/2}} = 0.62 \left(\frac{D_A}{\nu}\right)^{1/6} \left(\frac{\omega}{k_2 C_A^0}\right)^{1/2} \quad (19)$$

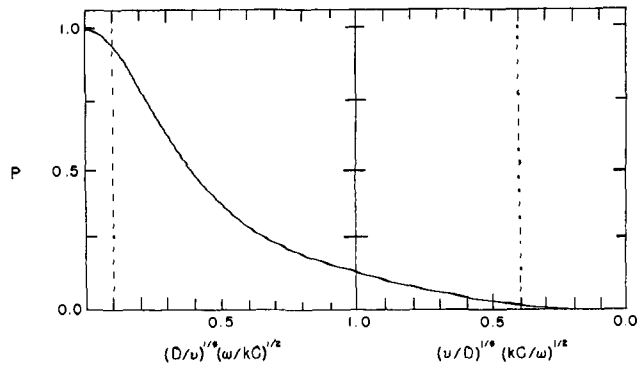

Figure 6. The probability of a fruitful encounter of B and C at the rrde.

or, upon rearrangement

$$I = 0.62\Phi_{ecl}A_D C_A^0 D_A^{2/3}\nu^{-1/6}\omega^{1/2} \quad (20)$$

This is quite similar to the Levich equation[13] for the rde for i_d, the current at the disk electrode

$$i_d = 0.62nFA_D C_A^0 D_A^{2/3}\nu^{-1/6}\omega^{1/2} \quad (21)$$

where n is the molar ratio of electrons to electroactive species and F is the faraday. Since the current at the disk is independent of conditions at the ring, (21) is valid even in rrde ecl, and combination of the simulation result of (20) with the Levich equation yields

$$I = \Phi_{ecl}(i_d/nF) \quad (22)$$

which is valid in the region of fast kinetics. Taking the point where

$$(D_A/\nu)^{1/6}(\omega/k_2C_A^0)^{1/2} = 0.1 \quad (23)$$

as the upper boundary of the region of fast kinetics, one obtains $\omega = 0.1k_2C_A^0$ as the rotation rate at this limit. This implies that if k_2 is greater than 10^7 M^{-1} sec^{-1}, the rrde assembly used here is incapable of rotation rates outside this limit, and (22) is always valid.

This consequence of a fast reaction between B and C is quite reasonable if one considers what can happen to a species B as it is swept across a ring which is generating species C: (1) it can react with C; (2) it can be converted to C at the ring electrode; (3) it can escape into the bulk of the solution. The result of the simulation in the limit of fast kinetics predicts that reaction with the ring-generated species C is the most probable of these three events. In Figure 6 this probability of fruitful encounter, P, is shown as a function of the dimensionless representation of ω in the manner of Figure 3. Note that in the region where (22) is valid, $P \approx 1.0$, so that in this region, essentially none of the B reaches the ring electrode or escapes into the bulk solution, and the disk current is an effective measure of the rate of a reaction occurring in the hydrodynamic layer.

The Effect of Instability of Radical Ions. The radical ions, represented by B and C in the simulation, may be unstable with respect to some decomposition reaction following the electrogeneration, and this instability affects the ecl behavior.[9b] For example 9,10-diphenylanthracene (DPA) cation radical is unstable in DMF solutions and decomposes by reaction with solvent and/or residual water. Typically, these reactions are taken into account in ecl studies by assuming that the decay occurs by a pseudo-first-order reaction

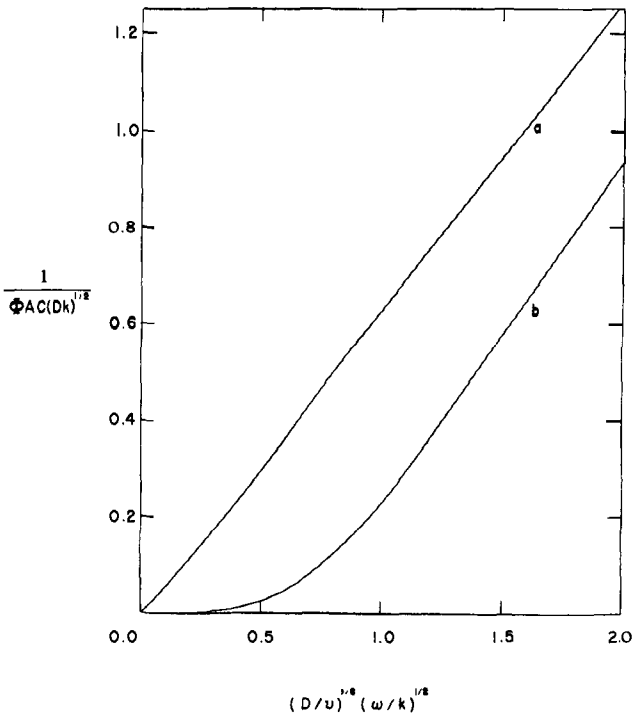

Figure 7. The effect of instability of B or C on the simulated intensity of ecl at the rrde: (a) result of generating unstable species at ring; (b) result of generating unstable species at disk.

$$B \xrightarrow{k_1} X \quad (24)$$

or

$$C \xrightarrow{k_1} X \quad (25)$$

These decompositions may also involve second-order (*e.g.*, coupling) or catalytic (*i.e.*, regeneration) reactions as well. The general method of simulating these is the same and the general behavior should be similar. The results of simulations including (24) or (25) are shown in Figure 7, where curve a shows the effect of an unstable ring-generated species (25) on the dimensionless I *vs.* $\omega^{1/2}$ behavior in rrde ecl, while curve b shows the effect of generating the unstable species at the disk (24). In either case, the reaction of B and C was considered fast with respect to the first-order decay ($k_2C_A^0 \geq 10^6k_1$) and I and ω were rendered dimensionless by k_1 rather than $k_2C_A^0$.

Curve a, of course, corresponds to the generation of $DPA\cdot^+$ at the ring, while b corresponds to the collection efficiency experiment where $DPA\cdot^+$ is generated at the disk. In both cases, the intensity in ecl is predicted to increase with increasing ω, but in the latter case, it is quite obvious that the effect of cation decay must be overcome before I is apparently linear with $\omega^{1/2}$. Thus, if I *vs.* $\omega^{1/2}$ is apparently linear but with a negative ordinate intercept, this can be attributed to the generation of an unstable species at the disk. On the other hand, the generation of the unstable species at the ring is much less likely to show this variation (although curve a is nonlinear). The important result to observe here is that at rotation rates where the disk generation of the unstable species causes an apparent negative intercept in the I *vs.* $\omega^{1/2}$ curve, the ring genera-

(13) V. G. Levich, "Physicochemical Hydrodynamics," Prentice-Hall, Englewood Cliffs, N. J., 1962.

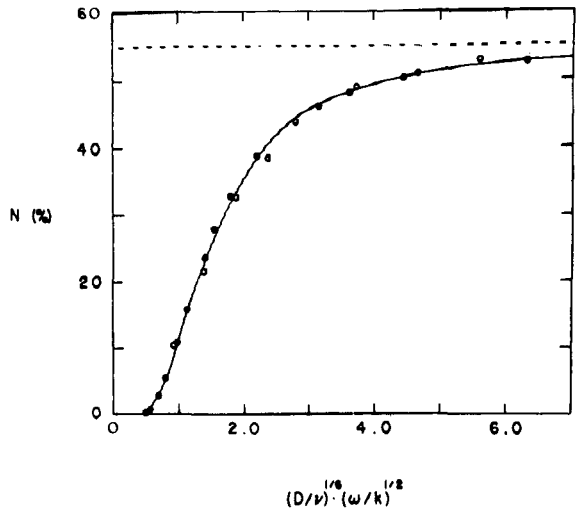

Figure 8. Collection efficiency, N, as a function of rotation rate: O, experimental points for the production of DPA·$^+$ at the disk and its reduction at the ring for a 1.0 mM DPA–0.1 M TBAP in DMF solution; ●, simulated results for a decomposition rate constant k_1 of 4.1 sec^{-1}.

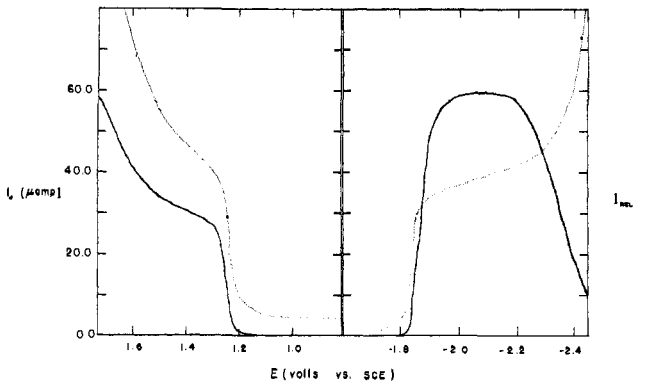

Figure 9. Steady-state current (···) and ecl intensity (—) as functions of disk potential for 1.0 mM DPA–0.1 M TBAP–DMF solution and ω = 132 sec^{-1}. For the scan on the left, the ring potential was maintained at about −2.1 V *vs.* sce; for the scan on the right, the ring potential was about +1.35 V *vs.* sce.

tion of that species will produce apparent I *vs.* $\omega^{1/2}$ behavior which extrapolates through the origin. This is a necessary condition if either one (but only one) of the ionic precursors of ecl undergoes reaction to form a product which is inactive to the other.

Discussion

The use of the rrde for ecl studies was tested using the system in DPA in 0.1 M tetrabutylammonium perchlorate (TBAP)-N,N-dimethylformamide (DMF) solutions. DPA was chosen as an initial test subject because its ecl emission spectrum agrees very well with its fluorescence spectrum, and no new fluorescent products appear from DPA solutions after electrolysis to produce ecl.[2] Its electrochemistry in DMF is known, and complications occur only upon DPA oxidation. Although the anion radical of DPA is stable in DMF solutions, the cation is unstable and is formed at potentials that lie close to those at which the TBAP–DMF solvent system is oxidized. Moreover, recent studies in this laboratory[14] indicate that there is no magnetic

(14) L. R. Faulkner and A. J. Bard, *J. Amer. Chem. Soc.*, **91**, 209 (1969).

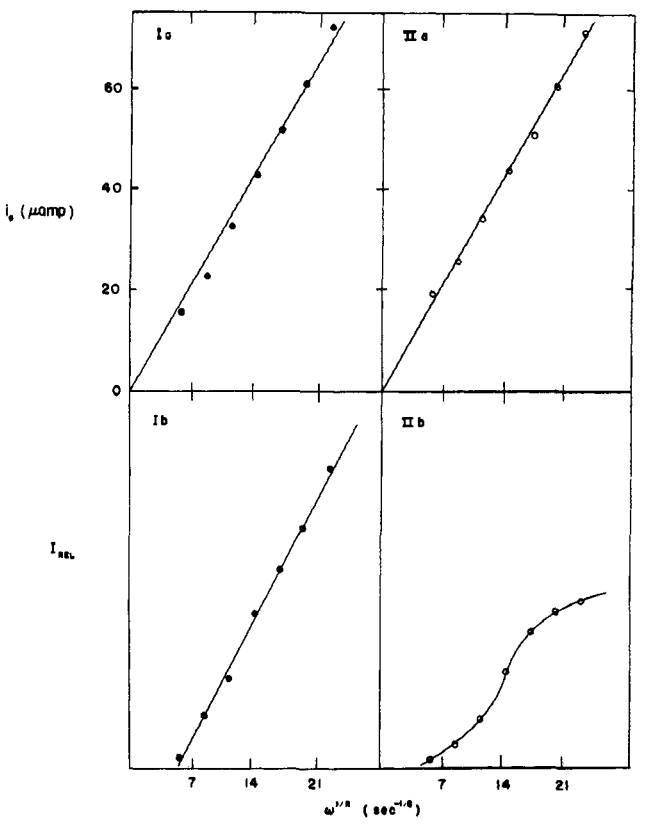

Figure 10. Limiting disk current and ecl intensity as functions of $\omega^{1/2}$ for 1.0 mM DPA–0.1 M TBAP–DMF solution: ● (Ia and Ib), reduction of DPA at disk; O (IIa and IIb), oxidation of DPA at disk.

field dependence on the intensity of ecl from the reaction of DPA·$^-$ and DPA·$^+$, but that there is a field dependence on the intensity of that resulting from the reaction of DPA·$^-$ and TMPD·$^+$ (Würster's Blue). This result has led to the hypothesis that ecl in a system containing only DPA does not involve triplet intermediates.

Results of various experiments of 1.0 mM DPA solutions at the rrde are shown in Figures 8–10. An experiment in which the disk is maintained at potentials where DPA·$^+$ is generated and the ring is maintained at a potential where only DPA·$^+$ is reduced is shown in Figure 8. The experimental collection efficiencies, N

$$N = |i_r/i_d| \qquad (26)$$

where i_r is the current at the ring electrode, are shown by the empty circles. In the absence of kinetic complications, N is independent of ω and is a constant for a given electrode. Smaller collection efficiencies result from decomposition of the disk generated species before it reaches the ring.[10,15] The behavior shown for DPA·$^+$ is characteristic of decomposition of DPA·$^+$. The line and filled circles in Figure 8 are results of a digital simulation[10] assuming a first-order decomposition of DPA·$^+$ with a rate constant of 4.1 sec^{-1}. Hence, the lifetime of the DPA cation in DMF was found to be 0.25 sec by this study. This lifetime is considerably longer than that reported previously from this laboratory;[9b] the two measurements were made using different

(15) W. J. Albery and S. Bruckenstein, *Trans. Faraday Soc.*, **62**, 1920, 1946 (1966).

techniques and the solutions were prepared from solvents purified in a different manner. This increase in cation lifetime probably reflects improvements made in the solvent-purification process.

The results of two potential scan experiments that were performed on a 1.0 m*M* solution of DPA in DMF with 0.1 *M* TBAP supporting electrolyte are shown in Figure 9. An identical rotation rate was used for each scan. The recordings on the left show the simultaneous ecl intensity and disk current behavior as a function of disk potential as the disk was scanned slowly through potentials which would oxidize DPA while the ring was held at potentials which would reduce DPA under limiting current conditions. Those at the right show the result of scanning the disk through the reduction of DPA while maintaining the ring at potentials which could bring about DPA oxidation. Current is shown as a dotted line in each scan and the relative ecl intensity is shown as a solid line.

These graphs are typical of those which were obtained at various rotation rates with the DPA system, and in all cases several observations are valid. (1) The limiting disk current at fixed ω is the same for both the oxidation and the reduction of DPA; a larger background current correction is required for oxidation, however. (2) No ecl is observed at these photomultiplier sensitivities from the generation of either $DPA\cdot^-$ or $DPA\cdot^+$ alone; hence, there is no background correction for ecl. This observation does not rule out low-level emission that might be observable at more sensitive photomultiplier settings, however, and in fact, this phenomenon was observed occasionally when a single species was generated in a solution which had previously been used for extensive electrolysis. (3) Ecl emission is proportional to the disk current so that the intensity–potential curves increase and go through a limiting region in a way similar to the current behavior in disk voltammetry. Any apparent lag in ecl behavior is probably because the potential was scanned as quickly as possible for a steady-state experiment ($\sim$0.5 V/min) so that the difference represents the delay in achieving steady-state conditions. (4) The limiting intensity of the ecl emission caused by generating $DPA\cdot^-$ at the disk is greater than that caused by the disk generation of $DPA\cdot^+$. Since the limiting current is the same in both cases, this indicates that the apparent efficiency of the anion is greater than that of the cation, because of the instability of the cation. (5) At high negative potentials the current increases as either DPA^{2-} is formed or the solvent system is reduced. At a rotating platinum electrode there is no indication of a limiting current that corresponds to the formation of the dianion, but its formation can be observed on a mercury electrode[16] at potentials close to those at which the solvent reduces on platinum. Since the ecl intensity actually decreases at these potentials, it appears that either $DPA\cdot^-$ is essential to the ecl process or that the product of TBAP–DMF reduction or DPA^{2-} is a quencher of ecl. (6) An opposite effect may be observed in the oxidation process, where the generation of the oxidation product of the TBAP–DMF system actually increases the ecl emission. This observation generally supports the contention that many oxidants will produce ecl by reaction with the DPA radical anion.

The effects of variations in rotation rate on the limiting current and the limiting relative ecl emission are shown in Figure 10. In this figure quadrant Ia shows the limiting disk current for DPA reduction as a function of $\omega^{1/2}$, while quadrant IIa shows this variation for the limiting disk current for DPA oxidation. Both i *vs.* $\omega^{1/2}$ curves exhibit straight line behavior passing through origin with essentially the same slope; this is in accord with Levich behavior as predicted by (21). In the lower quadrants of Figure 10, the limiting relative intensity of ecl emission for each process is plotted as a function of $\omega^{1/2}$ directly beneath the corresponding current plot. In general, three observations may be made about the I *vs.* $\omega^{1/2}$ behavior of DPA. (1) The ecl observed when DPA is reduced at the disk is linear with $\omega^{1/2}$. This linearity over the whole available range of ω indicates that the reaction between $DPA\cdot^-$ and $DPA\cdot^+$ is very rapid. It has been suggested that this redox reaction occurs at diffusion-controlled rates,[9a] and if this rate is calculated with the equation of Osborne and Porter[17]

$$k_0 = 8RT/2000\eta \qquad (27)$$

with η = 0.79 cP for DMF, a rate constant of 1.3×10^{10} M^{-1} sec^{-1} is obtained. This is three orders of magnitude greater than the minimum rate constant required for (22) to be valid. Further evidence for the rapidity of the radical annihilation reaction is the appearance of the chemiluminescence. Photographs of the rrde during ecl show a ring of light, with the emission concentrated on the inner edge of the ring. (2) The ecl occurring when DPA is oxidized at the disk increases with $\omega^{1/2}$, but not in a linear fashion. This can be ascribed, at least partially, to the instability of $DPA\cdot^+$ in DMF. (3) Both curves deviate to some extent from the shape predicted from the digital simulation. The fact that the I *vs.* $\omega^{1/2}$ plots show negative intercepts when either $DPA\cdot^+$ or $DPA\cdot^-$ is generated at the disk could result from both radical ions being unstable. However, $DPA\cdot^-$ is known to be stable and in fact shows theoretical collection efficiencies, independent of ω. Moreover, similar results are observed for rubrene ecl at the rrde.[5] The fact that a certain critical disk current must be attained before the appearance of ecl can also be attributed to quenching of excited DPA by a residual level of quencher, either impurity or solution component, so that a certain number of excited DPA molecules are needed to "titrate" the reaction zone to remove singlet quencher. The leveling of the I–$\omega^{1/2}$ curve when $DPA\cdot^+$ is generated at the disk at higher rotation rates could be caused by quenching of excited DPA molecules by $DPA\cdot^+$. Ecl efficiency measurements on this system[5] also suggest that quenching processes are of major importance in a complete description of the process.

A few experiments were performed using acetonitrile as the solvent, since its oxidative background limits are more positive than those of DMF and $DPA\cdot^+$ is more stable in this medium. In acetonitrile the general I–$\omega^{1/2}$ behavior was the same as that in DMF, although the data were more widely scattered. The intensity I

(16) K. S. V. Santhanam and A. J. Bard, *J. Amer. Chem. Soc.*, 88, 2669 (1966).

(17) A. D. Osborne and G. Porter, *Proc. Roy. Soc., Ser. A*, **220**, 104 (1953).

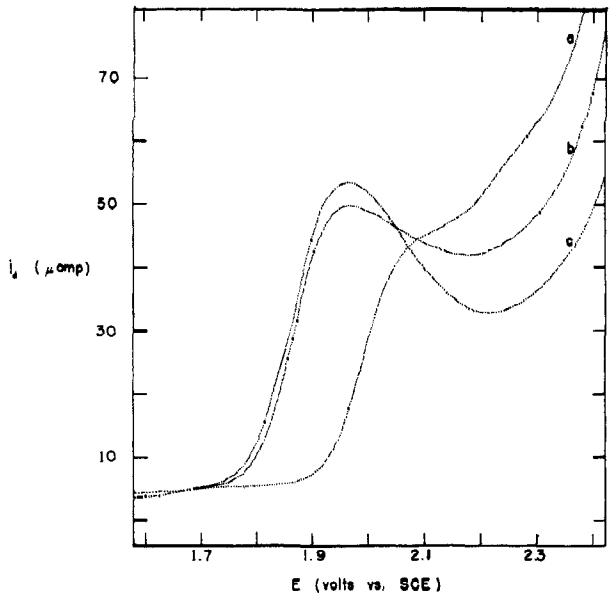

Figure 11. Rde voltammograms for the reduction of DPA in a 1.0 m*M* DPA–0.1 *M* acetonitrile solution for $\omega = 132$ sec^{-1}. Curves a, b, and c represent repeated cathodic scans with curve a taken following oxidation of DPA at disk electrode.

at a given disk current was somewhat higher when DPA$\cdot^+$ was generated at the disk; this is opposite to what is observed in DMF solutions. A voltammetric investigation of the reduction of DPA at the rotating-disk electrode (Figure 11) showed that these effects were caused by an electrode surface effect during reduction. The voltammograms shown in Figure 11 were all recorded at a rotation rate corresponding to $\omega = 132$ sec^{-1}; the alphabetization is in chronological order. Curve a was preceded by DPA oxidation at the electrode; its observed displacement in the negative direction could be the result of some surface phenomenon that is eliminated only at negative potentials. The effect shown by curve a and its cause are not critical to this discussion; they are only included here as an illustration of how electrode pretreatment can influence voltammetry. More important is the behavior exhibited by curves b and c which were obtained subsequent to curve a. Here it may be observed that the limiting current actually decreases with increasing potential; this suggests some type of filming reaction occurs which limits the flux of material into the electrode. This hypothesis was further substantiated by the appearance of a visible film on the electrode following DPA electrolysis in acetonitrile.

This filming need not be caused by DPA directly to interfere with DPA reductions. It may be that acetonitrile itself, catalyzed by the presence of DPA$\cdot^-$, polymerizes to film the electrode. Whatever the cause, however, the effect is serious enough to limit the flux of R$\cdot^-$ coming from either electrode in the rrde-ecl experiment.

Acknowledgment. The support of the Robert A. Welch Foundation and the U. S. Army Research Office-Durham is gratefully acknowledged.

Electrogenerated Chemiluminescence. VI. Studies of the Efficiency and Mechanisms of 9,10-Diphenylanthracene, Rubrene, and Pyrene Systems at a Rotating-Ring–Disk Electrode

J. T. Maloy and Allen J. Bard*[1]

Contribution from the Department of Chemistry, The University of Texas at Austin, Austin, Texas 78712.
Received January 13, 1971

Abstract: The actinometric calibration of the rotating-ring–disk electrode (rrde) system allowed the determination of the electrogenerated chemiluminescence (ecl) efficiency, Φ_{ecl}, for several systems of interest. The efficiency for 9,10-diphenylanthracene (DPA) ecl in dimethylformamide solutions was below 0.1%. Studies performed on the DPA–tetramethyl-*p*-phenylenediamine (TMPD) system showed that ecl occurs during reaction of DPA$\cdot^-$ with either TMPD$\cdot^+$ or TMPD^{2+}; the efficiency for this ecl is about an order of magnitude smaller than for DPA alone. TMPD was also shown to be an effective quencher of DPA ecl in these systems. Rrde studies of the rubrene (R) system demonstrated that Φ_{ecl} was much smaller for it than for the DPA system and that reaction of R^{2+} with R$\cdot^-$ or R^{2-} with R$\cdot^+$ produced light at high rotation rates. A detailed study of the pyrene (P)–TMPD system was undertaken. The Φ_{ecl} for the P–TMPD system was smaller than that for the DPA–TMPD system. A study of the relative pyrene excimer to monomer emission in both ecl and fluorescence demonstrated the existence of a direct path to excimer in ecl, consistent with the triplet–triplet annihilation mechanism. Quenching of pyrene ecl by TMPD was also investigated.

It is of considerable interest in studies of electrogenerated chemiluminescence (ecl) to determine the overall ecl efficiency, Φ_{ecl}, which represents the fraction of radical ion encounters which ultimately result in the emission of a photon. Studies of ecl at the rotating-ring–disk electrode (rrde) are ideally suited for such efficiency measurements, since the radical ion precursers are generated continuously under steady-state

(1) To whom correspondence and requests for reprints should be directed.